RAA 2021 Vol. **21** No. **8**, 208(16pp) doi: 10.1088/1674-4527/21/8/208

http://www.raa-journal.org *http://iopscience.iop.org/raa*

***R**esearch in*
***A**stronomy and*
***A**strophysics*

Studying infall in infrared dark clouds with multiple HCO^+ transitions

Jin-Jin Xie (谢津津)[1,2,3], Jing-Wen Wu (吴京文)[2,1], Gary A. Fuller[3,4], Nicolas Peretto[6], Zhi-Yuan Ren (任致远)[1], Long-Fei Chen (陈龙飞)[1], Yao-Ting Yan (闫耀庭)[7], Guo-Dong Li (李国栋)[1,2], Yan Duan (段言)[1,2], Ji-Feng Xia (夏季风)[1,2], Yong-Xiong Wang (王永雄)[3] and Di Li (李荻)[1,2,5]

[1] National Astronomical Observatories, Chinese Academy of Sciences, Beijing 100101, China; *jingwen@nao.cas.cn, dili@nao.cas.cn*
[2] University of Chinese Academy of Sciences, Beijing 100049, China
[3] Jodrell Bank Centre for Astrophysics, Department of Physics & Astronomy, The University of Manchester, Manchester M13 9PL, United Kingdom
[4] I. Physikalisches Institut, University of Cologne, Zülpicher Str. 77, 50937 Köln, Germany
[5] NAOC-UKZN Computational Astrophysics Centre, University of KwaZulu-Natal, Durban 4000, South Africa
[6] School of Physics & Astronomy, Cardiff University, Queen's Building, The Parade, Cardiff, CF24 3AA, United Kingdom
[7] Max-Planck-Institut für Radioastronomie, Auf dem Hügel 69, 53121 Bonn, Germany

Received 2021 March 3; accepted 2021 April 9

Abstract We investigate the infall properties in a sample of 11 infrared dark clouds (IRDCs) showing blue-asymmetry signatures in HCO^+ J=1–0 line profiles. We used JCMT to conduct mapping observations in HCO^+ J=4–3 as well as single-point observations in HCO^+ J=3–2, towards 23 clumps in these IRDCs. We applied the HILL model to fit these observations and derived infall velocities in the range of 0.5−2.7 km s^{-1}, with a median value of 1.0 km s^{-1}, and obtained mass accretion rates of 0.5–14 $\times 10^{-3}$ $M_\odot$ yr^{-1}. These values are comparable to those found in massive star forming clumps in later evolutionary stages. These IRDC clumps are more likely to form star clusters. HCO^+ J=3–2 and HCO^+ J=1–0 were shown to trace infall signatures well in these IRDCs with comparable inferred properties. HCO^+ J=4–3, on the other hand, exhibits infall signatures only in a few very massive clumps, due to smaller opacities. No obvious correlation for these clumps was found between infall velocity and the NH_3/CCS ratio.

Key words: stars: formation — ISM: clouds — star formation: kinematics and dynamics

1 INTRODUCTION

Mass accumulation by inward gravitational motions is a basic step in models of star formation (e.g. Larson 1969; Anglada et al. 1987; Bonnell et al. 2001; Motte et al. 2018). Infall motions often are revealed in observations with moderate optical depth molecular lines, which display blue-shifted self-absorption dips at frequencies where optically thin lines peak, produced by the temperature gradients of dense cores and the infalling gas (e.g. Walker et al. 1986; Wu & Evans 2003). Multiple transitions of many molecules such as CS, CO, H_2CO, HCO^+, HCN, CH_3CN and C_3H_2 have been investigated to search for infall signatures in various environments in low mass star forming regions (e.g. Myers et al. 1995; Mardones et al. 1997; Tafalla et al. 1998; Keown et al. 2016), as well as massive star forming regions (e.g. Zhang et al. 1998; Wu & Evans 2003; Fuller et al. 2005; Velusamy et al. 2008; Barnes et al. 2010; Qin et al. 2016).

The comparisons of different tracers including multiple transitions of the same tracer have been made through both observations and simulations, to explore which tracers are more efficient to reveal infall signatures in what kind of sources. Higher-J transitions, such as J=3–2 and J=4–3, of HCN and HCO^+ are considered as good tracers for dense clusters based on their infall asymmetries in lines generated in numerical simulations (Chira et al. 2014). Observationally, HCN J=3–2 has been considered as a very good infall tracer in a dense clump sample associated with H_2O masers (Wu & Evans 2003). The J=1–0

transition of HCN was found to have the strongest infall signatures (Stahler & Yen 2010) in simulations although the line shapes depend on the viewing angle (Smith et al. 2012). Compared to HCN, HCO^+ changes less drastically in abundances in chemical models at temperatures ranging from 10 K to 40 K (Vasyunina et al. 2012), which is the temperature range of dark clouds. Thus, HCO^+ is potentially better for comparing infall in different star forming environments as it is less affected by chemistry. Among HCO^+, the lowest transition, HCO^+ J=1–0, exhibited the most blue-asymmetric profiles towards a sample of 77 candidate high mass protostellar objects (HMPOs) (Fuller et al. 2005), which is consistent with the results of numerical simulations that HCO^+ J=1–0 is a better indicator of collapse in high mass star formation (Smith et al. 2013) where the gas is not dense enough to excite the higher-J transitions.

Being cold and dense, infrared dark clouds (IRDCs) are believed to represent the initial conditions of massive star formation and the formation of the associated stellar clusters (e.g. Carey et al. 2000; Rathborne et al. 2006; Peretto & Fuller 2009; Motte et al. 2018). Some pilot HCO^+ observations towards two massive IRDCs have revealed that the clumps/cores in there are undergoing rapid collapse (Peretto et al. 2013; Contreras et al. 2018). Considering IRDCs are at an earlier stage than HMPOs or ultracompact HII (UCHII) massive clumps, it raises the question of what molecular or ion line tracers can best trace infall in IRDCs? Specifically, will lower-J transitions with smaller critical density (like HCO^+ J=1–0) reveal infall signature better, or are higher-J transitions needed to probe collapse in these IRDCs? In addition, it is important to understand the properties of infall in the IRDC phase compared with infall in more evolved regions.

Recently, in an HCO^+ J=1–0 mapping survey towards a sample of 27 IRDCs (Peretto et al. in preparation), a significant fraction presented infall signatures in their line profiles. In this paper, we report our follow-up study on a sub-sample of these IRDCs, all of which show infall signatures in HCO^+ J=1–0 in at least one clump in the IRDCs. We mapped 11 IRDCs with HCO^+ J=4–3, and made single-point observations with HCO^+ J=3–2, towards 23 HCO^+ J =4–3 peak positions, using the James Clerk Maxwell Telescope (JCMT). The aims of the study are to use multiple HCO^+ transitions to fit and constrain models of infall motion, to understand infall properties in IRDCs, and to investigate if higher-J transitions of HCO^+ can also probe infall and reveal infall properties well in these HCO^+ J=1–0 selected IRDCs.

The organization of the rest of the paper is as follows: We describe source selection and observations in Section 2. The observational results and data analysis are presented in Section 3. We discuss infall tracers and infall properties of IRDCs in Section 4, and summarize our conclusions in Section 5.

2 TARGET SELECTION AND SPECTROSCOPIC OBSERVATIONS

The sources in this work are a sub-sample of an Institut de Radioastronomie Millimétrique (IRAM) 30 m HCO^+ J=1–0 survey towards 27 IRDCs (Peretto et al. in preparation). The parent sample was selected to span a range of geometries and a factor of $\sim$100 in mass ranging from $\sim$200 to $\sim 2\times10^4\,M_\odot$, to cover a representative sample of IRDCs. From the parent sample we selected 11 IRDCs that manifest blue asymmetry indicative of infall in HCO^+ J=1–0 in at least one clump. We made follow-up higher-J HCO^+ observations and we fit multiple transitions with models, in order to study infall properties in these candidate infalling IRDCs. The basic information on the sources is listed in Table 1.

All the sources have been mapped in HCO^+ J=1–0 with the IRAM 30 m telescope (half power beam width (HPBW): 29″; $\eta_{\rm mb}$=0.75). Since N_2H^+ J=1–0 has been found to be in good agreement with $H^{13}CO^+$ J=1–0 in both velocity and line width (Fuller et al. 2005), we rely on N_2H^+ J=1–0, which was observed simultaneously with HCO^+ J=1–0, to locate the central velocity of the cloud and to identify infall signature for all the HCO^+ transitions. The IRAM 30 m observations and data reduction of HCO^+ J=1–0 and N_2H^+ J=1–0 of the 27 IRDCs will be presented in a separated paper (Peretto et al. in preparation).

Eleven IRDCs were mapped in HCO^+ J=4–3 with the Heterodyne Array Receiver Programme (HARP)[1] (Buckle et al. 2009) (HPBW: 14″; $\eta_{\rm mb}$=0.63) on the 15 m JCMT[2] on Mauna Kea, Hawaii during August and September 2016 (Project M16BP081), and August 2017 (Project M17BP087). The Auto-Correlation Spectral Imaging System (ACSIS) spectrometer was employed. Maps of 180″ by 180″ (except one source SDC18.624, whose map size is 240″ × 180″) were made with RASTER scans with $T_{\rm sys}$ ranging from 364 K to 613 K (with an average of 443 K), under weather Band 3 and Band 4 with $0.08 < \tau_{225\,\rm GHz} < 0.20$.

Single-point observations were carried out in HCO^+ J=3–2 towards the HCO^+ J=4–3 peak positions

[1] https://www.eaobservatory.org/jcmt/instrumentation/heterodyne/harp/.

[2] The JCMT is operated by the East Asian Observatory (EAO) on behalf of NAOJ; ASIAA; KASI; CAMS as well as the National Key R&D Program of China (No. 2017YFA0402700). Additional funding support is provided by the STFC and participating universities in the UK and Canada.

with JCMT RxA3m frontend and ACSIS backend[3] (HPBW: 20″; $\eta_{\rm mb}$=0.57) from April to June 2018 under Project M18AP073. No $H^{13}CO^+$ J=3–2 observations were available due to a low LO current at 260 GHz. The molecule line frequencies are listed in Table 2. Each position was observed in position-switching mode (GRID) for an integration time of 300 s in weather Band 4 ($0.12 < \tau_{225\,\rm GHz} < 0.2$). An off-position (+600″, +600″) (J2000) from the observed position was also observed. The system temperatures ranged from 778 K to 1356 K, with an average of 988 K. For both the HARP and RxA3m observations, ACSIS was configured to cover 250 MHz wide windows, with 8192 channels in each window, resulting in a velocity resolution of $\sim$ 0.02 km s^{-1} for HARP and $\sim$ 0.03 km s^{-1} for RxA3m. All data for the HARP and RxA3 observations were smoothed with a Gaussian kernel which has full width at half maximum (FWHM) of 5.9 channels, resulting in a velocity resolution of 0.15 km s^{-1} and 0.20 km s^{-1} for HARP and RxA3, respectively. The telescope pointing was checked before observing a new source and was checked every 1–1.5 h, by observing one or more calibration sources in CO(2–1) at 234.591 GHz and CO(3–2) at 350.862 GHz for RxA3m and HARP, respectively. The uncertainty in the flux calibration is estimated to be about 10%.

The HARP and RxA3m data reduction were undertaken utilizing the STARLINK (Currie et al. 2014) software packages SMURF, KAPPA and GAIA. Each integration was first visually checked. The data were converted to spectral cubes and baselines were subtracted before being written out as FITS format files using standard STARLINK routines (Jenness et al. 2015).

All data were converted from the antenna temperature scale T_A^* to main-beam brightness temperature $T_{\rm mb}$ using $T_{\rm mb} = T_A^*/\eta_{\rm mb}$, where main beam efficiencies are listed in Table 2, as well as the noise levels and the velocity resolutions.

3 RESULTS

3.1 Infall Signature Statistics

We have mapped HCO^+ J=4–3 towards 11 IRDCs, which are presented as a contour map overlaid on the emission image of HCO^+ J=1–0 in Figure A.1 through Figure A.11 in Appendix A. The HCO^+ J=4–3 data have been convolved with the IRAM 30 m beam size. We identified 23 dense clumps based on HCO^+ J=4–3 emission peaks in the maps. These are labeled A through D in the figures. The coordinates of these peaks are tabulated in Table 4.

[3] https://www.eaobservatory.org/jcmt/instrumentation/heterodyne/rxa/

Table 1 Physical Parameters of the Observed IRDCs

Source Name	R.A.(J2000) (hh:mm:ss)	Decl.(J2000) (° ′ ″)	Distance[a] (kpc)	V_{LSR} (km s^{-1})
SDC18.624-0.070	18:25:10.0	–12:43:45	3.50	45.6
SDC18.888-0.476	18:27:09.7	–12:41:32	4.38	66.3
SDC22.373+0.446	18:30:24.5	–09:10:34	3.61	53.0
SDC23.367-0.288	18:34:53.8	–08:38:00	4.60	78.3
SDC24.489-0.689	18:38:25.7	–07:49:36	3.28	48.1
SDC24.618-0.323	18:37:22.4	–07:32:18	3.04	43.4
SDC25.166-0.306	18:38:13.0	–07:03:00	3.95	63.6
SDC28.333+0.063	18:42:54.1	–04:02:30	4.56	79.3
SDC35.429+0.138	18:55:30.4	+02:17:10	4.67	77.0
SDC35.527-0.269	18:57:08.6	+02:09:08	2.95	45.4
SDC35.745+0.147	18:56:02.6	+02:34:14	5.11	83.4

Notes: The coordinates and V_{LSR} are taken from Peretto et al. (in preparation). [a]The distances are determined from the Galactic Ring Survey (GRS) (Jackson et al. 2008).

The positions of the HCO^+ J=4–3 peaks generally agree well with HCO^+ J=1–0 peaks. An exception is SDC28.333+0.063, in which HCO^+ J=4–3 has peaks at two positions (B and C in the figure) without corresponding HCO^+ J=1–0 peaks. These two clumps may be very small in size and smoothed out by the much larger beam size in the IRAM 30 m telescope, or these regions may have quite different physical conditions leading to an unusual HCO^+ J=4–3 to HCO^+ J=1–0 ratio.

We present the spectra of all three transitions towards the peak positions in Appendix A. As seen from these spectra, infall signatures can be recognized in most of these clumps, and vary among different transitions. We categorized the profile signatures into five types that suggest different kinematic statuses: (1) double peaks with blue strong, an example can be seen in HCO^+ J=3–2 in SDC18.624-0.070B (see Fig. A.1); (2) a blue profile with a shoulder, e.g. the profile of HCO^+ J=4–3 in SDC18.624-0.070B (see Fig. A.1); (3) symmetric profile, e.g., HCO^+ J =3–2 in SDC18.624–0.070A (see Fig. A.1); (4) a red profile with a shoulder, e.g., HCO^+ J=1–0 in SDC18.888–0.476A (see Fig. A.2); (5) double peaks with red strong, e.g., HCO^+ J=3–2 in SDC18.888–0.476A (see Fig. A.2). We summarize the line profiles of different HCO^+ transitions for the 23 IRDC clumps in Table 3.

A double peak with a stronger blue peak profile is the best infall signature that indicates infall is ongoing and can be fitted to derive the infall properties. A blue peak with a red shoulder is also an infall signature which, although less dramatic, can still be used to derive infall parameters through modeling. Both profiles are called blue profiles. It is clear both from spectra or from Table 3 that HCO^+ J=1–0 has the best performance in revealing infall in these IRDCs, with 12 out of 23 displaying a double peak profile with blue peak strong, and five with a blue peak with a shoulder. This is not surprising given that this sample has a selection bias featuring blue asymmetry in

Table 2 Molecular Line Properties

Molecular Line	Frequency (GHz)	Telescope	$\eta_{\rm mb}$	HPBW	δv^a (km s^{-1})	Average rms^a (K)	Observation Date
HCO^+ J=1–0	89.18852470	IRAM 30 m	0.75	29″	0.16	0.07	2013^b
HCO^+ J=3–2	267.55762590	JCMT	0.57	20″	0.20	0.33	2018
HCO^+ J=4–3	356.73422300	JCMT	0.63	14″	0.15	0.25	2016, 2017

[a] Both δv and root mean square (rms) are on $T_{\rm mb}$ scale. All data were smoothed with a Gaussian kernel with FWHM of 5.9 channels. [b] The IRAM 30 m observations of HCO^+ J=1–0 were made by Peretto et al. (in prep).

HCO^+ J=1–0. HCO^+ J=3–2 presents a less prominent, yet still comparable, ability to reveal blue profiles, with 11 out of 23 having double peaks with the blue peak stronger, and three blue peaks with red shoulder profiles. HCO^+ J=4–3 only presents profiles with double peaks and the blue peak stronger in three clumps, and shows a blue peak with a shoulder in 13 clumps. It is less sensitive in revealing infall in this IRDC sample. More discussion to compare the ability of the three transitions to reveal infall will be given in Section 4.

3.2 Infall Velocity Calculations

To derive the infall parameters, we adopted the HILL model (De Vries & Myers 2005) to fit the spectral lines. The HILL model is based on the precursor 'two-layer' model (Myers et al. 1996), which has been adopted in many infall studies, though the 'two-layer' model has been found to underestimate infall velocity by a factor of ∼2 (De Vries & Myers 2005). The HILL model assumes a hill shape excitation temperature profile across the cloud, where the center has the peak excitation temperature T_P (De Vries & Myers 2005). The brightness temperature of the molecular line is

$$\begin{aligned}\Delta T_B\left(v\right) = &\left(J\left(T_P\right) - J\left(T_0\right)\right)\left[\left(1-\mathrm{e}^{-\tau_f(v)}\right)\Big/\tau_f\left(v\right)\right.\\ &\left.-\mathrm{e}^{-\tau_f(v)}\left(1-\mathrm{e}^{-\tau_r(v)}\right)\Big/\tau_r\left(v\right)\right]\\ &+\left(J\left(T_0\right)-J\left(T_b\right)\right)\left[1-\mathrm{e}^{-\tau_r(v)-\tau_f(v)}\right],\end{aligned} \quad (1)$$

where T_B is the brightness temperature defined as $T_B = \left(c^2\Big/2\nu^2 k\right) I_v$, and I_ν is the specific intensity. The excitation temperature at the outer edges of the core is T_0. The optical depth τ_f is the optical depth where the excitation temperature is rising along the line of sight and τ_r is the opposite, with a velocity dispersion of σ for the entire cloud. We developed a Python fitting code which consists of five parameters, i.e., the HILL5 model, based on Equation (1)[4] using Python package LMFIT[5], which also provides error estimates. HILL5 is the HILL model with five free parameters, which are optical depth τ, infall velocity $V_{\rm in}$, systematic velocity $V_{\rm LSR}$, velocity dispersion σ and excitation temperature $T_{\rm ex}$. HILL5 is considered as the most robust model among the HILL models (De Vries & Myers 2005), and has been applied to calculate infall velocities in various objects such as IRDCs (e.g. Contreras et al. 2018), low mass cores (e.g. Maureira et al. 2017) and massive starless clumps (e.g. Calahan et al. 2018).

We applied the HILL5 model to fit HCO^+ J=1–0, 3–2 and 4–3 spectral lines towards the peak positions as listed in Table 4. Fitted lines are plotted in red in Figure A.1 through Figure A.11. The fitted infall velocities are listed in Table 4. We exclude clumps (SDC18.888-0.476A, SDC24.618 and SDC35.429) which have red-asymmetries for all transitions.

In some sources (e.g., SDC25.166–0.306C), although the blue-asymmetric profile looks different for different transitions, the derived infall velocities are similar ($\Delta V_{\rm in} < 0.2$ km s^{-1}). A possible explanation is that the line has different optical depth, as listed in Table 4, which causes differences in the line profiles, even with similar infall velocities.

3.3 Clump Sizes and Line Luminosities from HCO^+ J=4–3 Maps

HCO^+ J=4–3 traces the densest part of the cloud among the three transitions, thus it can be used to define the compact, very dense regions in these IRDCs. We obtained the effective angular diameter ($\theta_{\rm transition}$) size of the dense clumps by measuring the area of the contour at the intensity which is half of the peak intensity of HCO^+ J=4–3, following the method applied in Wu et al. (2010), with the equation

$$\theta_{\rm transition} = 2\left(\frac{A_{1/2}}{\pi} - \frac{\theta_{\rm beam}^2}{4}\right)^{1/2}, \quad (2)$$

where $A_{1/2}$ is the area within the contour of half-peak intensity and $\theta_{\rm beam}$ is the angular beam size. $R_{\rm transition}$ is the equivalent spatial radius of the clumps, and is calculated as $R_{\rm transition} = \theta_{\rm transition} D/2$, where D is the distance of the source.

[4] This equation is typeset incorrectly in the Astrophysical Journal in (De Vries & Myers 2005). The correct version can be found in the arXiv version in 2004arXiv: astro-ph/0410748.

[5] https://lmfit-py.readthedocs.io/

Table 3 The Numbers of Clump Profile Signatures

Profile Signatures	HCO^+ J=1–0	HCO^+ J=3–2	HCO^+ J=4–3
Double Peaks with Blue Strong	12	11	3
Blue Profile with Shoulder	5	3	13
Symmetric	2	4	2
Red Profile with Shoulder	3	1	1
Double Peaks with Red Strong	0	4	2

Table 4 Infall Velocities Fitted by HILL at Peak Positions of HCO^+ J=4–3

Source Name	R.A.(J2000)	Decl.(J2000)	HCO^+ J=1–0			HCO^+ J=3–2			HCO^+ J=4–3		
	(hh:mm:ss)	(° ′ ″)	V_{in} (km s^{-1})	σ (km s^{-1})	τ	V_{in} (km s^{-1})	σ (km s^{-1})	τ	V_{in} (km s^{-1})	σ (km s^{-1})	τ
SDC18.624-0.070A	18:25:10.8	-12:42:20	$0.85^{+0.19}_{-0.16}$	$1.42^{+0.09}_{-0.08}$	$2.60^{+0.36}_{-0.35}$	$0.31^{+0.11}_{-0.13}$	$1.36^{+0.03}_{-0.03}$	$0.96^{0.06}_{0.03}$	-	-	-
SDC18.624-0.070B	18:25:08.5	-12:45:25	$1.33^{+0.05}_{-0.06}$	$0.82^{+0.03}_{-0.02}$	$7.99^{+0.01}_{-0.18}$	$1.47^{+0.15}_{-0.15}$	$1.21^{+0.10}_{-0.09}$	$4.21^{+0.59}_{-0.49}$	$0.74^{+0.15}_{-0.26}$	$1.16^{+0.21}_{-0.13}$	$0.79^{+0.41}_{-0.20}$
SDC18.888-0.476A	18:27:09.7	-12:41:32	-	-	-	-	-	-	-	-	-
SDC18.888-0.476B	18:27:07.1	-12:41:40	$0.57^{+0.21}_{-0.28}$	$1.87^{+0.07}_{-0.09}$	$0.53^{+0.03}_{-0.02}$	$1.88^{+0.11}_{-0.11}$	$2.00^{+0.01}_{-0.50}$	$1.21^{+0.05}_{-0.05}$	$0.85^{+0.10}_{-0.27}$	$2.33^{+0.10}_{-0.03}$	$0.35^{+0.02}_{-0.02}$
SDC22.373+0.446	18:30:24.5	-09:10:34	$0.97^{+0.10}_{-0.10}$	$0.84^{+0.05}_{-0.05}$	$2.88^{+0.35}_{-0.33}$	$0.94^{+0.13}_{-0.15}$	$0.75^{+0.08}_{-0.07}$	$4.63^{+1.08}_{-0.85}$	$0.77^{+0.15}_{-0.12}$	$0.89^{+0.52}_{-0.66}$	$2.09^{+0.30}_{-0.32}$
SDC23.367-0.288A	18:34:53.9	-08:38:22	$1.16^{+0.34}_{-0.31}$	$2.45^{+0.12}_{-0.23}$	$0.50^{+0.15}_{-0.05}$	$1.47^{+0.37}_{-0.43}$	$2.00^{+0.06}_{-0.59}$	$0.32^{+0.04}_{-0.03}$	$0.81^{+0.20}_{-0.44}$	$1.15^{+0.21}_{-0.13}$	$0.81^{+0.49}_{0.56}$
SDC23.367-0.288B	18:34:52.4	-08:36:47	$1.35^{+0.40}_{-0.42}$	$1.13^{+0.20}_{-0.21}$	$3.17^{+1.22}_{-0.99}$	$1.30^{+0.71}_{-0.50}$	$1.45^{+0.23}_{-0.31}$	$2.40^{+0.93}_{-0.98}$	$1.32^{+0.20}_{-0.77}$	$0.97^{+0.22}_{-0.11}$	$2.10^{+1.04}_{-0.90}$
SDC24.489-0.689A	18:38:25.8	-07:49:36	$0.98^{+0.10}_{-0.10}$	$1.04^{+0.05}_{-0.05}$	$4.83^{+0.52}_{-0.47}$	$0.49^{+0.21}_{-0.16}$	$0.97^{+0.08}_{-0.07}$	$5.09^{+1.19}_{-1.00}$	$0.80^{+0.38}_{-0.26}$	$1.28^{+0.13}_{-0.17}$	$1.40^{+0.40}_{-0.56}$
SDC24.489-0.689B	18:38:28.4	-07:49:05	$1.85^{+0.14}_{-0.13}$	$1.24^{+0.09}_{-0.08}$	$5.37^{+0.90}_{-0.72}$	-	-	-	-	-	-
SDC24.618-0.323A	18:37:22.9	-07:31:42	-	-	-	-	-	-	-	-	-
SDC24.618-0.323B	18:37:21.5	-07:33:20	-	-	-	-	-	-	-	-	-
SDC25.166-0.306A	18:38:09.7	-07:02:31	$0.79^{+0.09}_{-0.08}$	$1.20^{+0.04}_{-0.04}$	$3.68^{+0.30}_{-0.28}$	-	-	-	-	-	-
SDC25.166-0.306B	18:38:18.1	-07:02:52	$0.61^{+0.09}_{-0.08}$	$1.05^{+0.05}_{-0.05}$	$5.09^{+0.57}_{-0.52}$	$0.56^{+0.14}_{-0.12}$	$0.82^{+0.06}_{-0.06}$	$5.67^{+1.39}_{-1.11}$	$0.60^{+0.20}_{-0.23}$	$0.92^{+0.15}_{-0.12}$	$1.09^{+0.50}_{-0.30}$
SDC25.166-0.306C	18:38:13.1	-07:03:08	$0.88^{+0.12}_{-0.11}$	$1.10^{+0.05}_{-0.05}$	$4.24^{+0.47}_{-0.44}$	$0.68^{+0.73}_{-0.30}$	$0.88^{+0.16}_{-0.27}$	$3.87^{+1.87}_{-1.97}$	$0.49^{+0.13}_{-0.30}$	$0.97^{+0.07}_{-0.13}$	$0.80^{+0.16}_{-0.10}$
SDC28.333+0.063A	18:42:50.7	-04:03:14	$0.45^{+0.11}_{-0.16}$	$1.00^{+0.01}_{-0.01}$	$0.80^{+0.03}_{-0.03}$	$1.47^{+0.25}_{-0.23}$	$1.44^{+0.11}_{-0.12}$	$6.38^{+2.01}_{-1.46}$	$0.79^{+0.13}_{-0.14}$	$1.23^{+0.08}_{-0.07}$	$1.02^{+0.20}_{-0.20}$
SDC28.333+0.063B	18:42:52.2	-03:59:56	-	-	-	$1.52^{+0.34}_{-0.26}$	$1.43^{+0.15}_{-0.14}$	$3.99^{+0.87}_{-0.76}$	$0.37^{+0.07}_{-0.07}$	$1.14^{+0.04}_{-0.04}$	$5.38^{+0.55}_{-0.50}$
SDC28.333+0.063C	18:42:54.1	-04:02:30	$0.77^{+0.32}_{-0.28}$	$2.92^{+0.20}_{-0.17}$	$5.54^{+1.09}_{-0.83}$	$0.09^{+0.34}_{-0.26}$	$0.74^{+0.13}_{-0.09}$	$2.03^{+0.98}_{-0.93}$	$0.34^{+0.13}_{-0.18}$	$1.20^{+0.04}_{-0.09}$	$0.80^{+0.04}_{-0.02}$
SDC28.333+0.063D	18:42:49.3	-04:02:17	$2.70^{+0.33}_{-0.31}$	$2.20^{+0.23}_{-0.22}$	$7.09^{+2.24}_{-1.52}$	$1.31^{+0.38}_{-0.33}$	$1.20^{+0.15}_{-0.15}$	$4.49^{+1.47}_{-1.16}$	$0.46^{+0.32}_{-0.77}$	$1.45^{+0.12}_{-0.18}$	$0.30^{+0.23}_{-0.02}$
SDC35.429+0.138	18:55:34.1	+02:19:07	-	-	-	$0.70^{+0.16}_{-0.60}$	$1.18^{+0.23}_{-0.14}$	$0.47^{+0.40}_{-0.20}$	-	-	-
SDC35.527-0.269A	18:57:09.1	+02:07:55	$1.03^{+0.14}_{-0.16}$	$1.35^{+0.13}_{-0.10}$	$1.29^{+0.32}_{-0.35}$	$0.87^{+0.12}_{-0.01}$	$0.62^{+0.01}_{-0.09}$	$1.00^{+0.10}_{-0.07}$	$0.32^{+0.13}_{-0.47}$	$0.81^{+0.05}_{-0.13}$	$0.80^{+0.35}_{-0.20}$
SDC35.527-0.269B	18:57:08.0	+02:10:56	$0.56^{+0.26}_{-0.29}$	$1.01^{+0.11}_{-0.12}$	$0.83^{+0.31}_{-0.49}$	$0.54^{+0.15}_{-0.51}$	$0.60^{+0.26}_{-0.15}$	$0.98^{+0.01}_{-0.85}$	$0.22^{+0.41}_{-0.82}$	$1.03^{+0.13}_{-0.25}$	$0.10^{+0.51}_{-0.35}$
SDC35.527-0.269C	18:57:08.6	+02:09:07	$0.90^{+0.30}_{-0.47}$	$1.19^{+0.24}_{-0.19}$	$1.28^{+0.63}_{-0.60}$	-	-	-	$0.51^{+0.40}_{-0.06}$	$1.11^{+0.18}_{-0.24}$	$0.80^{+0.45}_{-0.10}$
SDC35.745+0.147	18:56:01.7	+02:34:37	$0.54^{+0.08}_{-0.08}$	$1.36^{+0.05}_{-0.05}$	$3.06^{+0.26}_{-0.25}$	-	-	-	$-0.85^{+0.17}_{-0.20}$	$1.12^{+0.10}_{-0.10}$	$1.82^{+0.41}_{-0.42}$

The upper and lower limits of infall velocities are determined within 3σ confidence interval limit. We excluded the values from the profiles where there is no infall signature.

The line luminosity is then calculated as

$$L' = 23.5 \times 10^{-6} \times D^2 \times \left(\frac{\pi \times \theta^2_{\rm transition}}{4\ln 2}\right) \times \left(\frac{\theta^2_{\rm transition} + \theta^2_{\rm beam}}{\theta^2_{\rm transition}}\right) \times \int T_{mb}\ {\rm K\ km\ s^{-1}}, \quad (3)$$

where $T_{\rm mb}dv$ is the integrated intensity at the peak position, D is in kpc and θ in arcsec (Wu et al. 2010). The calculated clump angular sizes, spatial sizes R and line luminosities for HCO^+ J=4–3 are listed in Table 5.

These IRDC clumps have HCO^+ J =4–3 sizes ranging from 0.17 pc to 0.73 pc, with a mean size of 0.33 pc and a median size of 0.28 pc. These sizes are comparable to clump sizes of higher-J transitions found in later stages of massive clumps. For example, the half-peak clumps' sizes of HCN J=3–2 towards some UCHII clumps (Wu et al. 2010) have a mean and median size of 0.32 pc and 0.26 pc, respectively. The derived line luminosity of HCO^+ J =4–3 is in the range 0.2–18 K km s^{-1} pc^2, with a mean and median value of 4.1 K km s^{-1} pc^2 and 2.6 K km s^{-1} pc^2, respectively.

3.4 Clump Mass and Mass Accretion Rate

Assuming all the mass within the beam is uniformly distributed and contributing to the infall motions and the peak regions are spherical, following Calahan et al. (2018) the mass accretion rate is calculated as

$$\dot{M} = 4\pi R^2 \rho v_{\rm in} = \frac{3 M v_{\rm in}}{R} = 3068 \frac{M_\odot}{\rm Myr}\left(\frac{M}{1000\ M_\odot}\right)\left(\frac{v_{\rm in}}{1\ {\rm km\ s^{-1}}}\right)\left(\frac{1\ {\rm pc}}{R}\right). \quad (4)$$

The infall velocities used to calculate the mass accretion rates for these IRDCs are from the modeling of HCO^+ J=1–0 observations. We rely on the column density maps from Peretto et al. (2016) to calculate the mass then the average volume density of the clumps within the IRAM HCO^+ J=1–0 beam to match the radius from infall observations, to estimate the mass accretion rates. Peretto et al. (2016) derived the column density maps of the sources from *Herschel* 160 μm and 250 μm observations obtained as part of the Hi-GAL survey (Molinari et al.

Table 5 The Derived Parameters of IRDC Clumps

Source Name	Clump Size[a] ($''$)	$R_{\rm transition}$ [a] (pc)	Line Luminosity[a] (K km s^{-1} pc^2)	$\int T_{\rm mb} dv$[a] (K km s^{-1})	$\overline{N_{\rm H_2}}$[b] 10^{22} cm^{-2}	$M^{\rm b}_{\rm H_2}$ ($M_\odot$)	$\dot{M}^{\rm c}$ ($\times10^{-3}$ $M_\odot$ yr^{-1})
SDC18.624–0.070A	31	0.26	2.74	3.97	-	-	-
SDC18.624–0.070B	33	0.28	3.05	6.76	4.2	636	10.3
SDC18.888–0.476A	-	-	-	8.43	-	-	-
SDC18.888–0.476B	49	0.52	17.64	12.02	24.5	3430	28.4
SDC22.373+0.446	26	0.23	1.22	3.51	6.7	564	4.8
SDC23.367–0.288A	25	0.28	1.16	2.02	12.9	1597	10.6
SDC23.367–0.288B	15	0.17	0.42	1.46	1.1	288	1.2
SDC24.489–0.689A	51	0.41	4.13	4.35	8.3	426	4.4
SDC24.489–0.689B	-	-	-	2.41	-	-	-
SDC24.618–0.323A	37	0.27	2.35	5.24	-	-	-
SDC24.618–0.323B	-	-	-	2.16	-	-	-
SDC25.166–0.306A	47	0.45	4.32	3.00	-	-	-
SDC25.166–0.306B	-	-	-	1.95	4.9	734	2.1
SDC25.166–0.306C	-	-	-	1.56	5.1	830	3.1
SDC28.333+0.063A	25	0.28	2.04	4.56	5.4	420	4.8
SDC28.333+0.063B	35	0.39	5.90	6.99	-	-	-
SDC28.333+0.063C	-	-	-	3.09	4.1	291	5.8
SDC28.333+0.063D	-	-	-	3.16	3.7	275	19.8
SDC35.429+0.138	37	0.42	8.47	6.67	-	-	-
SDC35.527–0.269A	29	0.21	0.51	2.08	3.0	280	1.8
SDC35.527–0.269B	28	0.20	0.49	1.59	2.4	248	0.9
SDC35.527–0.269C	28	0.20	0.23	0.91	-	-	-
SDC35.745+0.147	59	0.73	11.50	3.79	-	-	-
Mean	35	0.33	4.13	3.99	6.6	770	7.5
Median	32	0.28	2.55	3.13	5.0	490	4.8

[a]The physical parameters are from HCO^+ J=4–3 observations. The clump size and $R_{\rm transition}$ are determined from half peak intensity of HCO^+ J=4–3 observations. For some sources, the sizes of half intensity contours are smaller than the beam size such that the sources are unresolved. Thus, we cannot calculate their sizes and masses. [b]The physical parameters are from *Herschel* 160 μm and 250 μm observations, see Sect. 3.4 for details. [c] The physical parameters are derived from HCO^+ J=4–3 observations, see Sect. 3.4 for details.

Table 6 Previous Infall Studies

Targets [a]	Tracer	Method	$V_{\rm in}$ Range (km s^{-1})	Mean $V_{\rm in}$ (km s^{-1})	$\dot{M}$ Range ($\times10^{-3} M_\odot$ yr^{-1})	Reference
HMPOs (22/77)	(1–0)	two-layer	[0.1, 1.0]	-	[0.2, 1.0]	[1]
UCHII (9/23)	(4–3)	two-layer	[0.1, 1.8]	∼0.9	[0.02, 10]	[2]
UCHII (8/30)	(3–2)	two-layer	[0.1, 1.3]	∼0.5	[0.03, 6]	[3]
BGPS clump (6/101)	(1–0)	HILL5	[0.3, 0.8]	∼0.7	[0.5, 2]	[4]
Hi-GAL clump (21/213)	(1–0)	two-layer	[0.2, 1.5]	∼0.3	[0.7, 45.8]	[5]
four IRDCs	(1–0)	two-layer	[0.4, 2.4]	∼1.0	[2.0, 18.0]	[6]
IRDCs	(1–0)	HILL5	[0.5, 2.7]	∼1.0	[2.0, 17.2]	This Work

The references are: [1] Fuller et al. (2005); [2] Klaassen & Wilson (2007); [3] Churchwell et al. (2010); [4] Calahan et al. (2018); [5] Traficante et al. (2018); [6] Giannetti et al. (2015). [a] The numbers in parentheses are the numbers of infall candidates versus the total numbers of sources. The infall velocity derived from the two-layer model has been found to be about a factor of 2 smaller than that calculated from the HILL5 model (De Vries & Myers 2005; Barnes et al. 2010).

2016) and they estimate an uncertainty of ∼50% in the column density (Peretto et al. 2016).

The assumption that all mass within the beam will contribute to infall profile could lead to an overestimate of the averaged volume density within the beam due to the foreground and background emission along the line of sight, therefore overestimating the mass accretion rate. The averaged column density within the beam, as well as the derived mass accretion rate of the sources, is listed in Table 5.

Note that the above mass estimated from the column density map within the IRAM beam is a beam-size defined mass. Here we want to estimate the physical mass of these clumps by calculating the total dust masses above 4σ of the *Herschel* map. Based on the radiative transfer equation, following Hildebrand (1983), the flux density of the dust core is related to its mass in the form of

$$\begin{aligned} S_\nu &= \kappa_\nu B_\nu(T_{\rm d}) \Omega \mu m_{\rm H} N_{\rm tot} \\ &= \frac{\kappa_\nu B_\nu(T_{\rm d}) M_\Omega}{D^2}, \end{aligned} \tag{5}$$

wherein S_ν is the flux density at the frequency ν. Ω is the solid angle of the core or selected area. $B_\nu(T_{\rm d})$ is the Planck function of the dust temperature $T_{\rm d}$ and $N_{\rm tot}$ is the gas column density (mostly HI+H_2). μ =

2.33 is the average molecular weight, $m_{\rm H}$ is the mass of the hydrogen atom and κ_ν is the dust opacity, which is assumed to be related to the frequency in the form $\kappa_\nu = \kappa_{230\rm GHz}(\nu/230\,\rm GHz)^\beta$. The reference value $\kappa_{230\rm GHz} = 0.009\ \rm cm^2\ g^{-1}$ is adopted from dust model for the grains with coagulation for 10^5 yr with accreted ice mantles at a density of $10^6\ \rm cm^{-3}$ (Ossenkopf & Henning 1994). D is the source distance. In calculation, we used the NH_3 kinetic temperature (Xie et al. 2021) to approximate the dust temperature. The total core mass which covers the regions above 4σ in the dust emission map have been calculated utilizing Equation (5), and the result is displayed in Table 5. The derived masses of these IRDC clumps range from 250 to 3400 $M_\odot$, with a mean mass of 770 $M_\odot$ and a median mass of 490 $M_\odot$. They are massive enough to form massive star clusters.

The mean and median values of the mass accretion rates are $7.5\times10^{-3}\,M_\odot\ \rm yr^{-1}$ and $4.8\times10^{-3}\,M_\odot\ \rm yr^{-1}$, respectively. These values are slightly larger than those found in later massive star forming regions like HMPOs or UCHII regions, as seen in Table 6. Given that the infall velocity derived from the two-layer model will be underestimated by a factor of 2 compared to the HILL5 model, the mass accretion rates in these IRDCs are not very different from those in HMPOs or UCHII regions.

The Kelvin-Helmholtz timescale, which is the time it takes for a star to radiate away its total kinetic energy, reflects how long a star can sustain its luminosity by gravitational contraction. An empirical form of the Kelvin-Helmholtz timescale $t_{\rm KH}$ can be written as (Li 2002)

$$t_{\rm KH} \approx 19{\rm Myr}\left(\frac{M_*}{M_\odot}\right)^{-2.5}, \qquad (6)$$

where M_* is the stellar mass. For a sufficiently massive star, $t_{\rm KH}$ can be too short for a star to even reach the main sequence (Li et al. 2003; Klaassen & Wilson 2007). For example, an $8\,M_\odot$ stellar mass, the lower end of massive stars, has a Kelvin-Helmholtz timescale of 0.1 Myr. The mass accretion rate has to be high enough to allow mass accumulated within 0.1 Myr to be more than $8\,M_\odot$, so that the massive star will survive to the main sequence. Our measured accretion rate of $5\times10^{-3}\,M_\odot\ \rm yr^{-1}$ in these IRDC clumps corresponds to the infall of $\sim500\,M_\odot$ in 0.1 Myr. According to Equation (6), for any stellar mass $M_* \lesssim 26\,M_\odot$, the current infall rate can provide enough accretion within its Kelvin-Helmholtz time, but it will be hard for more massive stars to reach the main sequence. Therefore, these IRDC clumps can form massive stars, but are more likely to form star clusters rather than a single massive star.

4 DISCUSSION

4.1 Infall Tracers for IRDCs

Some works have claimed that HCO^+ J=4–3 is likely more sensitive to trace infall than HCO^+ J=1–0 in massive star forming regions, especially for denser regions (Tsamis et al. 2008; Purcell et al. 2006; Klaassen et al. 2012). While in a survey towards a large sample of HMPOs, HCO^+ J=1–0 has been found to have more prominent infall signatures, i.e., double peaks with a self-absorbed dip, than HCO^+ J=4–3 lines (Fuller et al. 2005), suggesting lower-J HCO^+ transitions could be a better infall tracer in these regions. Very limited such studies have been done on IRDCs (e.g. Wyrowski et al. 2016). Based on our survey with multiple HCO^+ lines towards a sample of 23 clumps, we can evaluate their ability to reveal infall in IRDCs.

As seen from Table 3, the surveys with three HCO^+ transitions at least imply that in infall candidates selected by HCO^+ J =1–0, HCO^+ J=4–3 is not more sensitive, not even comparable, in detecting infall in IRDCs. These results suggest HCO^+ J =4–3 may not be optically thick enough to reveal infall in these IRDCs, as also indicated by the opacity derived from the HILL model in Table 4 and Figure 2.

HCO^+ J=3–2 has been found to have comparable ability to HCO^+ J=1–0 to study infall in later stages of massive star forming regions like HMPOs (Fuller et al. 2005; Reiter et al. 2011; Klaassen et al. 2012), and we find a similar trend for HCO^+ J=3–2 in IRDCs. As well as the line profiles, we also compare the derived infall velocities of the three HCO^+ transitions as presented in Table 4. The infall velocities derived from HCO^+ J=1–0 are slightly larger than those from HCO^+ J=3–2 overall, but the weighted average of both transitions is similar ($1.02\pm0.03\ \rm km\ s^{-1}$ for HCO^+ J=1–0 and $0.89\pm0.01\ \rm km\ s^{-1}$ for HCO^+ J=3–2). This may suggest that throughout the parts or layers in the clump where HCO^+ J=1–0 and 3–2 probe, the infall velocity does not change much, agreeing with the hypothesis that infall velocity is consistent within these layers or regions. The infall velocities of HCO^+ J=4–3, on the other hand, are much smaller. The weighted average infall velocity of HCO^+ J=4–3 ($0.67\pm0.05\ \rm km\ s^{-1}$) is more than 1.5 times smaller than what is derived from HCO^+ J=1–0, with a similar result being found in another study using the two-layer model towards an IRAS source (Barnes et al. 2010). Excluding the non-fitted and/or negative values in Table 4, the median values of infall velocities for HCO^+ J=1–0, 3–2 and 4–3 are 0.97, 0.94 and 0.74 $\rm km\ s^{-1}$, respectively. The comparisons between pairs of transitions of HCO^+ are depicted in Figure 1, which suggests that

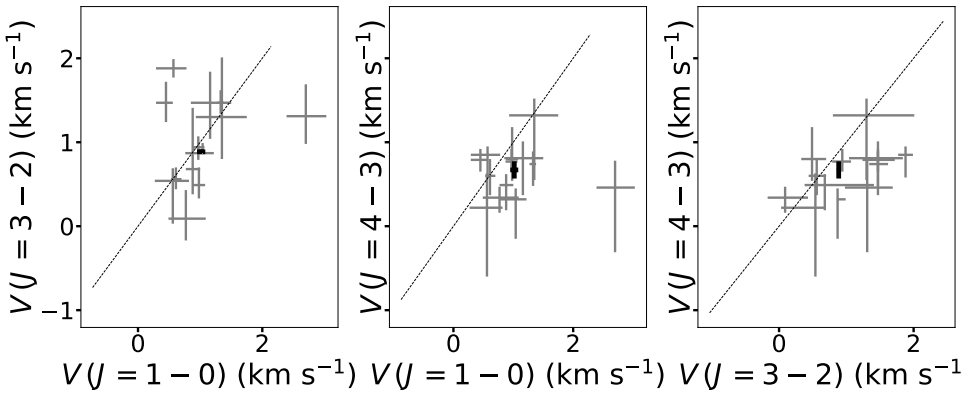

Fig. 1 The infall velocity comparisons among the three transitions: J=1–0, J=3–2 and J=4–3. The *diagonal line* indicates where the infall velocities are equal. The *black marks* signify the weighted average of infall velocities.

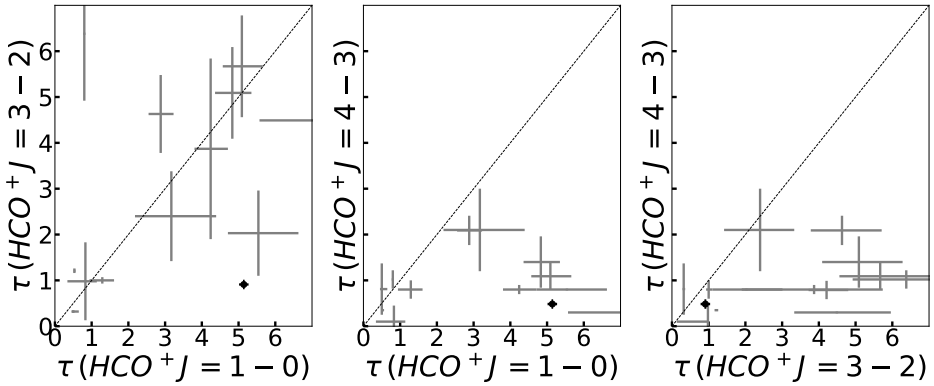

Fig. 2 The optical depth comparisons among the three transitions: J=1–0, J=3–2 and J=4–3. The *diagonal line* indicates where the optical depths are equal. The *black marks* signify the weighted average of optical depths. Despite the scattering of the optical depths of HCO^+ J=3–2 and HCO^+ J=1–0, they are similar and both are higher than those of HCO^+ J=4–3.

the infall velocity of HCO^+ J=3–2 is comparable to that of HCO^+ J=1–0, while both are larger than those of HCO^+ J=4–3. The opacities derived from the HILL5 model for all three transitions are also listed in Table 4, and are compared between every two transitions for each clump in Figure 2. It is clear to see that the opacities calculated from HCO^+ J=1–0 and 3–2 are comparable and both are much higher than the values from HCO^+ J=4–3. This is consistent with RADEX (van der Tak et al. 2007) modeling for 10^4–10^5 cm^{-3} at temperatures from 15 to 30 K. The detailed modeling is beyond the scope of this observational work and will be presented in future works.

4.2 Infall Properties of IRDCs

Different infall tracers, especially lower-J and higher-J HCO^+ or HCN transitions, normally trace different parts or layers of dense star forming clumps. For massive clumps at different evolutionary stages, like UCHII regions, HMPOs and IRDCs, we will need different infall tracers to best probe the collapsing regions in the clumps, as argued in Wu & Evans (2003) that the infall profile will best be revealed when the opacity of the source and the critical density of the tracer can be well matched. Therefore, the infall properties may be compared for samples at different evolutionary stages as long as the best infall tracers are used to model the kinematic information of infall.

Under this assumption, we find that the infall velocities of IRDCs obtained in this work are in general consistent with the values in other massive star forming regions. For example, an infall velocity of ∼1.5 km s^{-1} for HCO^+ J=3–2 was obtained applying the HILL5 model towards an IRDC (Contreras et al. 2018) with mass approximating the mass of SDC23.367-0.288, which has an average infall velocity of ∼1.4 km s^{-1}. In Table 6, we listed infall velocities as well as mass accretion rates obtained from some other studies towards HMPOs and UCHII regions, to compare with our results. Considering that infall velocities calculated from the two-layer model are generally a factor of 2 less than those obtained from the HILL model, the derived infall velocity and therefore the mass accretion rate of these IRDCs (with a median

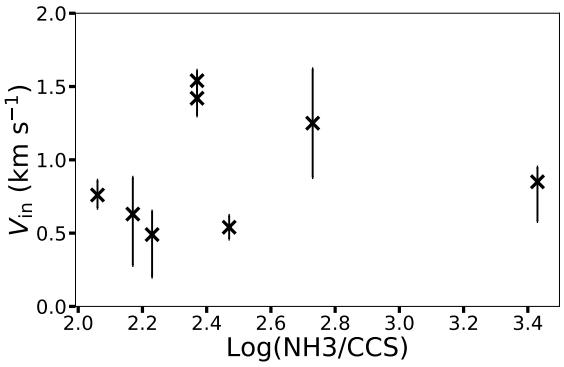

Fig. 3 Infall velocities versus the logarithm of the ratio of the column density of NH_3 to that of CCS.

of 1.0 km s^{-1}) is actually comparable to those calculated from HMPOs (Fuller et al. 2005) or UCHII regions (Klaassen & Wilson 2007), which is interesting as this suggests that although these molecular line tracers may originate from different parts/layers of the clumps, they imply that infall velocities are within a similar range for these different samples.

4.3 Infall Velocities and the NH_3 to CCS Ratio

Some works have argued that the ratio of the column densities of NH_3 and dicarbon sulfide (CCS) could be an indicator of chemical evolution in low mass and high mass star formation (e.g. Suzuki et al. 1992; Sakai et al. 2008). Should this ratio be an indicator of chemical evolution within the IRDC stage in massive star formation, we have tested to see if there is any correlation between the obtained infall velocity and the logarithm of the ratio of the column density of NH_3 to that of CCS. To best match the resolution of the NH_3 and CCS surveys (HPBW$\sim 45''$) (Xie et al. 2021), we use the infall velocities derived from HCO^+ J=1–0 (HPBW$\sim$ 30″). The results are featured in Figure 3. For the IRDCs in our sample, we see no obvious correlation between infall velocities and the logarithm of the ratio of the NH_3 column density to the CCS column density.

5 CONCLUSIONS

We summarize our main conclusions as the following:

1. We investigate the infall properties in a sample of 11 IRDCs which present infall line profiles in an HCO^+ J=1–0 survey by Peretto et al. (in prep). A total of 23 clumps were identified in HCO^+ J =4–3 maps of theses IRDCs and they were observed in HCO^+ J =3–2 using JCMT. The sizes and line luminosities of these IRDC clumps in HCO^+ J=4–3 were calculated.

2. We compare the infall signatures traced by the three transitions of HCO^+ towards the peaks of the 23 IRDC clumps and found that HCO^+ J =3–2 can trace infall signature well in this HCO^+ J =1–0 selected sample, while HCO^+ J =4–3 shows the least blue asymmetric profiles in these IRDCs.

3. We employed the HILL model to fit infall parameters based on the three HCO^+ transition profiles for the identified IRDC clumps. The infall velocities derived from HCO^+ J=1–0 range from 0.5 to 2.7 km s^{-1}, with a median of 1.0 km s^{-1}, which are similar to the values derived from HCO^+ J=3–2 and are more than 1.5 times larger than the values derived from HCO^+ J=4–3.

4. The infall velocities and the mass accretion rates in the IRDC clumps in our survey are comparable to the values found in HMPO and UCHII samples. These IRDC clumps are more likely to form star clusters.

5. No prominent correlation between the infall velocities and the ratio of NH_3 column density to CCS column density has been found in this sample.

Acknowledgements This work is supported by the National Natural Science Foundation of China (NSFC, Grant Nos. 11988101, 11725313 and 11721303), the International Partnership Program of Chinese Academy of Sciences (Grant No. 114A11KYSB20160008) and the National Key R&D Program of China (No. 2016YFA0400702). Xie J.J. acknowledges support by the Chinese Scholarship Council (CSC) and the STFC China SKA Exchange Programme for support as a visiting PhD student in the United Kingdom. G.A.F acknowledges support from the Collaborative Research Centre 956, funded by the Deutsche Forschungsgemeinschaft (DFG) project ID 184018867. The authors wish to recognize and acknowledge the very significant cultural role and reverence that the summit of Mauna Kea has always had within the indigenous Hawaiian community. We are most fortunate to have the opportunity to conduct observations from this mountain. Xie J.J. acknowledges support and help from the JCMT observing team, especially Jim Hoge, Kevin Silva, Dan Bintley and Mauna Kea Rangers. The STARLINK software (Currie et al. 2014) is currently supported by the East Asian Observatory. This research made use of APLPY, an open-source plotting package for Python (Robitaille & Bressert 2012; Robitaille 2019).

Appendix A: OBSERVATIONAL POSITIONS OF RXA3M OF HCO^+ J=3–2 ON THE EMISSION MAP OF HCO^+ J =1–0 WITH HCO^+ J=4-3 CONTOURS

References

Anglada, G., Rodriguez, L. F., Canto, J., Estalella, R., & Lopez,

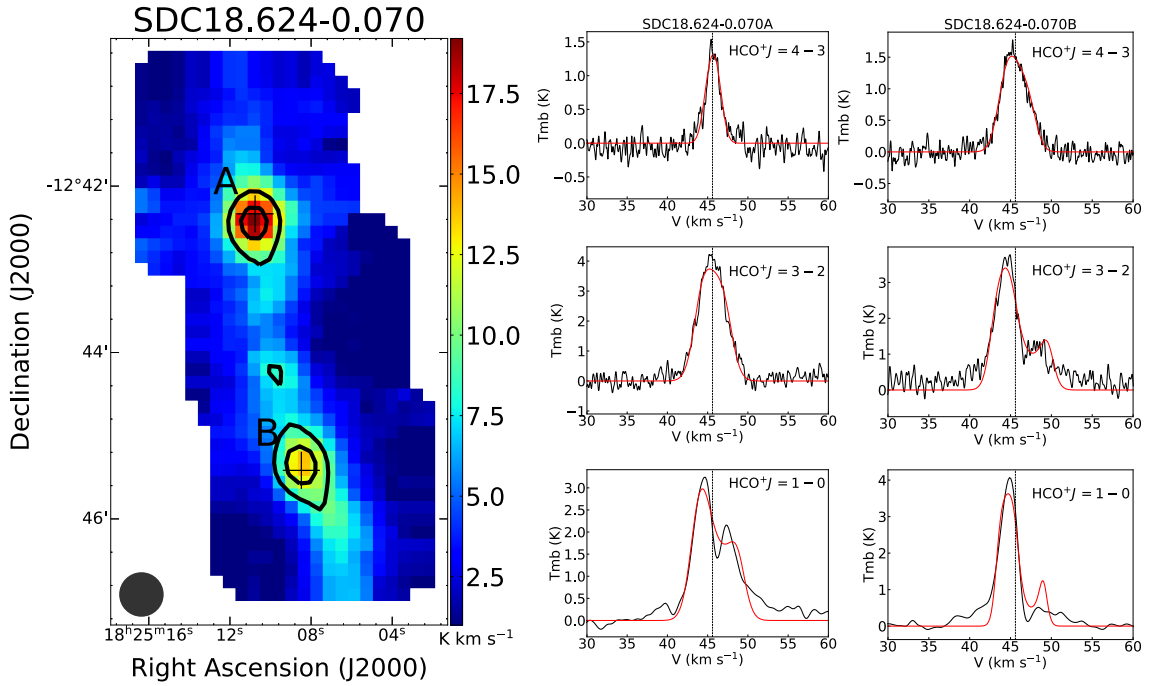

Fig. A.1 The integrated intensity map of HCO^+ J=1–0 overlaid with HCO^+ J=4–3 contours at 0.5, 0.8 and 1.0 of the maximum of the integrated intensity in K km s^{-1} for SDC18.624. The maximum of the integrated intensity has been stated in Table 5 as the biggest value of $\int T_{\rm mb} dv$ for the source. A and B are the observed positions of HCO^+ J=3–2. The spectra are fitted with the HILL model. The *black emission profiles* are from the data, while the *red lines* represent the fitted profiles. The *grey dot* at the corner of the emission map represents the IRAM beam size.

R. 1987, A&A, 186, 280
Barnes, P. J., Yonekura, Y., Ryder, S. D., et al. 2010, MNRAS, 402, 73
Bonnell, I. A., Bate, M. R., Clarke, C. J., & Pringle, J. E. 2001, MNRAS, 323, 785
Buckle, J. V., Hills, R. E., Smith, H., et al. 2009, MNRAS, 399, 1026
Calahan, J. K., Shirley, Y. L., Svoboda, B. E., et al. 2018, ApJ, 862, 63
Carey, S. J., Feldman, P. A., Redman, R. O., et al. 2000, ApJL, 543, L157
Chira, R.-A., Smith, R. J., Klessen, R. S., Stutz, A. M., & Shetty, R. 2014, MNRAS, 444, 874
Churchwell, E., Sievers, A., & Thum, C. 2010, A&A, 513, A9
Contreras, Y., Sanhueza, P., Jackson, J. M., et al. 2018, ApJ, 861, 14
Currie, M. J., Berry, D. S., Jenness, T., et al. 2014, in Astronomical Society of the Pacific Conference Series, Vol. 485, Astronomical Data Analysis Software and Systems XXIII, eds. N. Manset & P. Forshay, 391
De Vries, C. H., & Myers, P. C. 2005, ApJ, 620, 800
Fuller, G. A., Williams, S. J., & Sridharan, T. K. 2005, A&A, 442, 949
Giannetti, A., Wyrowski, F., Leurini, S., et al. 2015, A&A, 580, L7
Hildebrand, R. H. 1983, QJRAS, 24, 267
Jackson, J. M., Finn, S. C., Rathborne, J. M., Chambers, E. T., & Simon, R. 2008, ApJ, 680, 349
Jenness, T., Currie, M. J., Tilanus, R. P. J., et al. 2015, MNRAS, 453, 73
Keown, J., Schnee, S., Bourke, T. L., et al. 2016, ApJ, 833, 97
Klaassen, P. D., Testi, L., & Beuther, H. 2012, A&A, 538, A140
Klaassen, P. D., & Wilson, C. D. 2007, ApJ, 663, 1092
Larson, R. B. 1969, MNRAS, 145, 271
Li, D. 2002, Massive cores in the Orion molecular cloud, PhD thesis, CORNELL UNIVERSITY
Li, D., Goldsmith, P. F., & Menten, K. 2003, ApJ, 587, 262
Mardones, D., Myers, P. C., Tafalla, M., et al. 1997, ApJ, 489, 719
Maureira, M. J., Arce, H. G., Dunham, M. M., et al. 2017, ApJ, 838, 60
Molinari, S., Schisano, E., Elia, D., et al. 2016, A&A, 591, A149
Motte, F., Bontemps, S., & Louvet, F. 2018, ARA&A, 56, 41
Myers, P. C., Bachiller, R., Caselli, P., et al. 1995, ApJL, 449, L65
Myers, P. C., Mardones, D., Tafalla, M., Williams, J. P., & Wilner, D. J. 1996, ApJL, 465, L133
Ossenkopf, V., & Henning, T. 1994, A&A, 291, 943
Peretto, N., & Fuller, G. A. 2009, A&A, 505, 405
Peretto, N., Lenfestey, C., Fuller, G. A., et al. 2016, A&A, 590, A72
Peretto, N., Fuller, G. A., Duarte-Cabral, A., et al. 2013, A&A, 555, A112

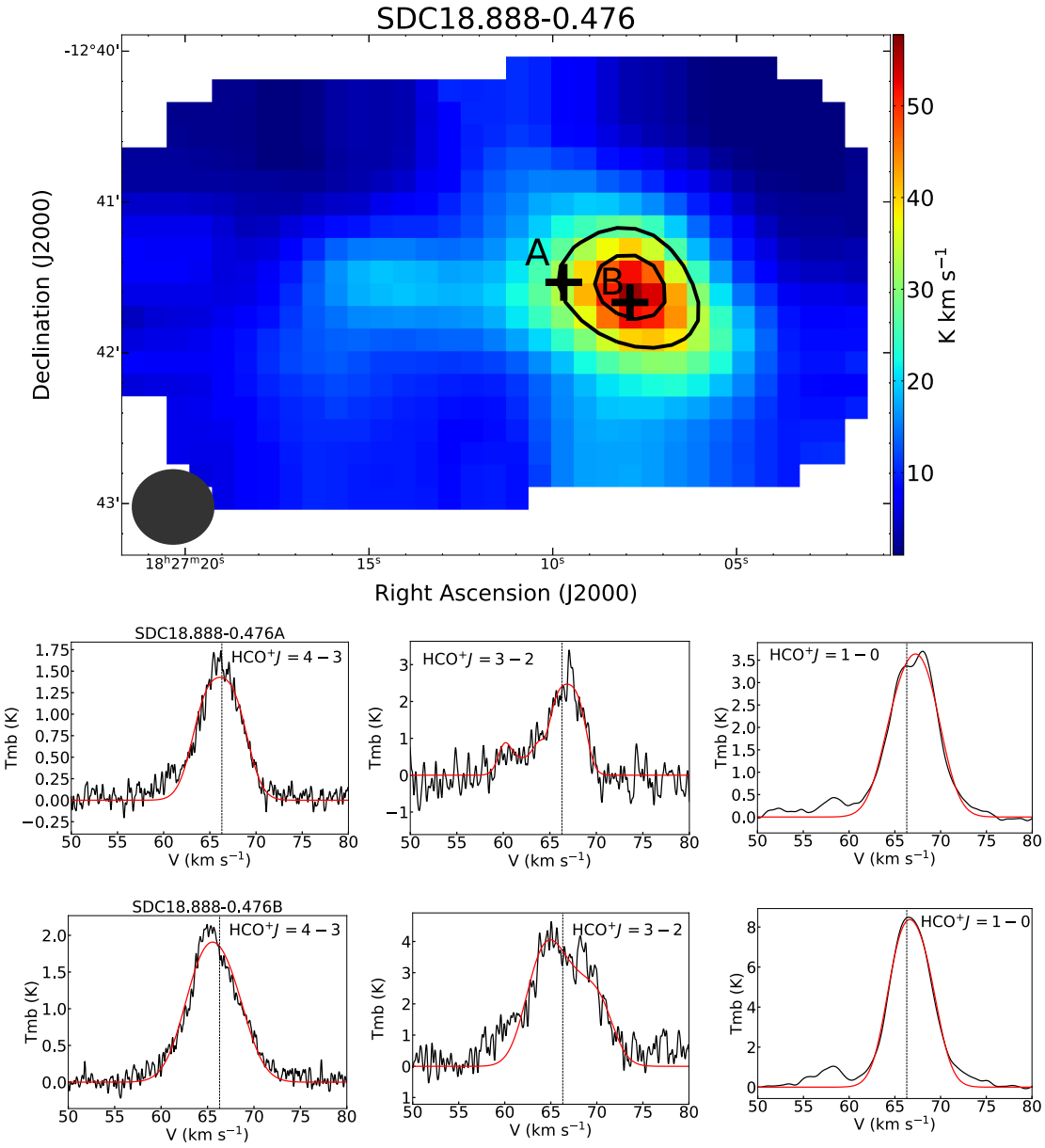

Fig. A.2 The integrated intensity map of HCO^+ J=1–0 overlaid with HCO^+ J=4–3 contours at 0.5, 0.8 and 1.0 of the maximum of the integrated intensity in K km s^{-1} for SDC18.888. The maximum of the integrated intensity has been stated in Table 5 as the biggest value of $\int T_{\rm mb} dv$ for the source. A and B are the observed positions of HCO^+ J=3–2. The *grey dot* at the corner of the emission map represents the IRAM beam size.

Purcell, C. R., Balasubramanyam, R., Burton, M. G., et al. 2006, MNRAS, 367, 553
Qin, S.-L., Schilke, P., Wu, J., et al. 2016, MNRAS, 456, 2681
Rathborne, J. M., Jackson, J. M., & Simon, R. 2006, ApJ, 641, 389
Reiter, M., Shirley, Y. L., Wu, J., et al. 2011, ApJ, 740, 40
Robitaille, T. 2019, APLpy v2.0: The Astronomical Plotting Library in Python, https://doi.org/10.5281/zenodo.2567476
Robitaille, T., & Bressert, E. 2012, APLpy: Astronomical Plotting Library in Python, Astrophysics Source Code Library, ascl:1208.017
Sakai, T., Sakai, N., Kamegai, K., et al. 2008, ApJ, 678, 1049
Smith, R. J., Shetty, R., Beuther, H., Klessen, R. S., & Bonnell, I. A. 2013, ApJ, 771, 24
Smith, R. J., Shetty, R., Stutz, A. M., & Klessen, R. S. 2012, ApJ, 750, 64
Stahler, S. W., & Yen, J. J. 2010, MNRAS, 407, 2434
Suzuki, H., Yamamoto, S., Ohishi, M., et al. 1992, ApJ, 392, 551

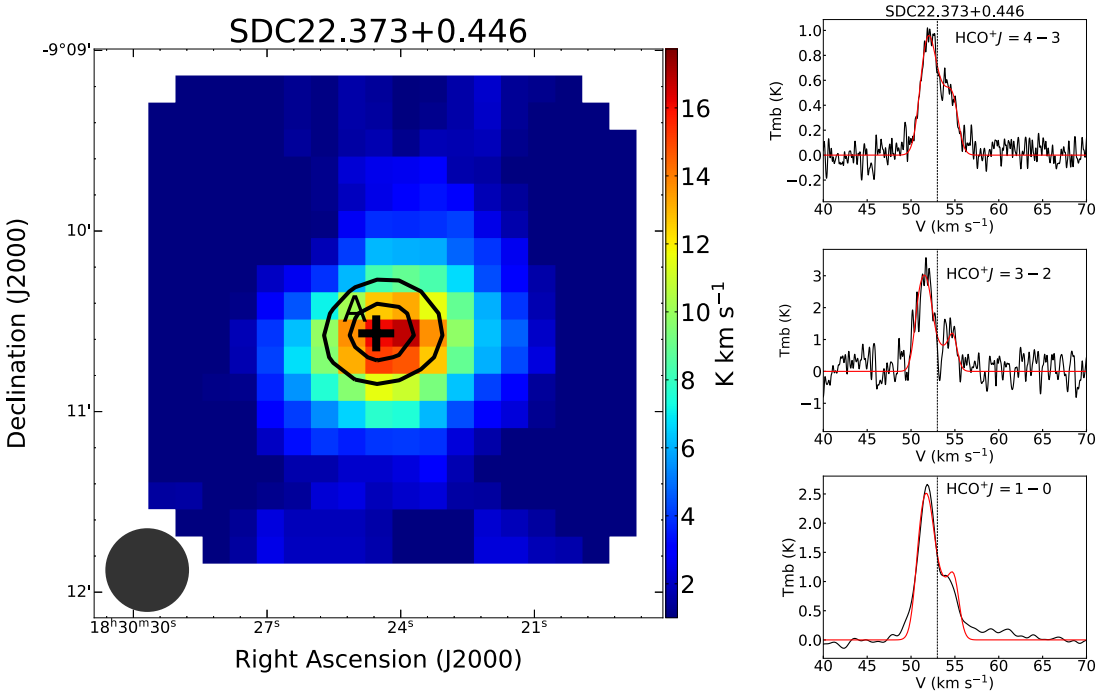

Fig. A.3 The integrated intensity map of HCO^+ J=1–0 overlaid with HCO^+ J=4–3 contours at 0.5, 0.8 and 1.0 of the maximum of the integrated intensity in K km s^{-1} for SDC22.373. The maximum of the integrated intensity has been stated in Table 5 as the biggest value of $\int T_{\rm mb} dv$ for the source. A is the observed positions of HCO^+ J=3–2. The *grey dot* at the corner of the emission map represents the IRAM beam size.

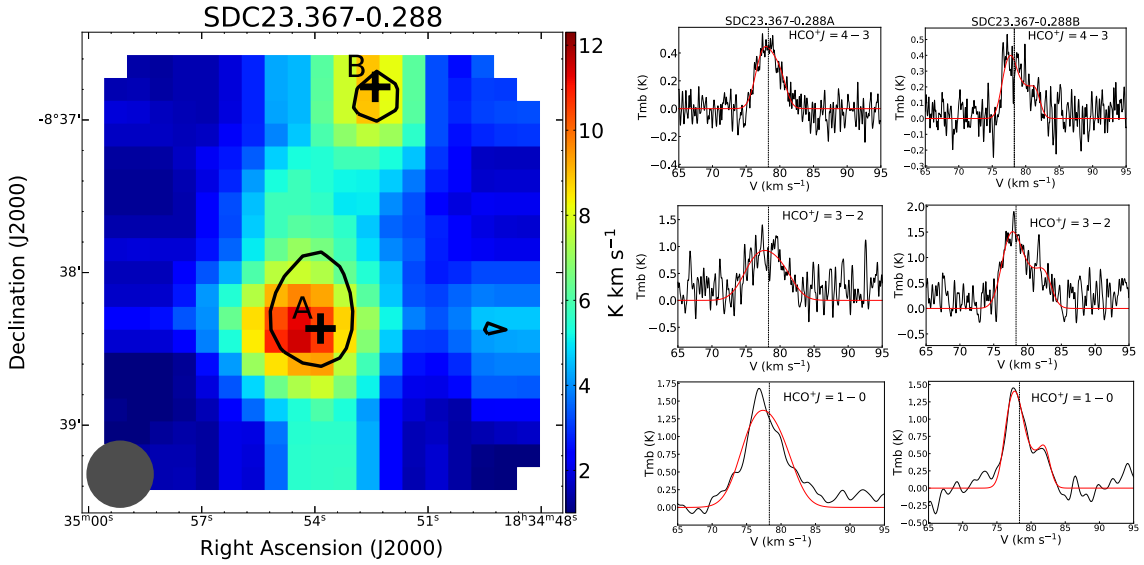

Fig. A.4 The integrated intensity map of HCO^+ J=1–0 overlaid with HCO^+ J=4–3 contours at 0.5, 0.8 and 1.0 of the maximum of the integrated intensity in K km s^{-1} for SDC23.367. The maximum of the integrated intensity has been stated in Table 5 as the biggest value of $\int T_{\rm mb} dv$ for the source. A and B are the observed positions of HCO^+ J=3–2. The *grey dot* at the corner of the emission map represents the IRAM beam size.

Tafalla, M., Mardones, D., Myers, P. C., et al. 1998, ApJ, 504, 900

Traficante, A., Duarte-Cabral, A., Elia, D., et al. 2018, MNRAS, 477, 2220

Tsamis, Y. G., Rawlings, J. M. C., Yates, J. A., & Viti, S. 2008, MNRAS, 388, 898

van der Tak, F. F. S., Black, J. H., Schöier, F. L., Jansen, D. J., & van Dishoeck, E. F. 2007, A&A, 468, 627

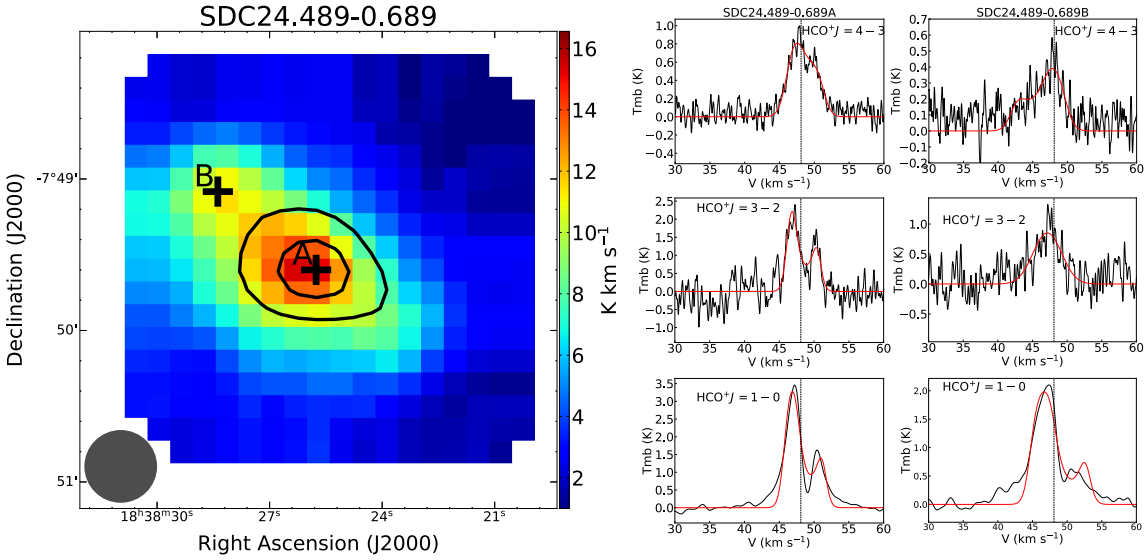

Fig. A.5 The integrated intensity map of HCO^+ J=1–0 overlaid with HCO^+ J=4–3 contours at 0.5, 0.8 and 1.0 of the maximum of the integrated intensity in K km s^{-1} for SDC24.489. The maximum of the integrated intensity has been stated in Table 5 as the biggest value of $\int T_{\rm mb} dv$ for the source. A and B are the observed positions of HCO^+ J=3–2. The *grey dot* at the corner of the emission map represents the IRAM beam size.

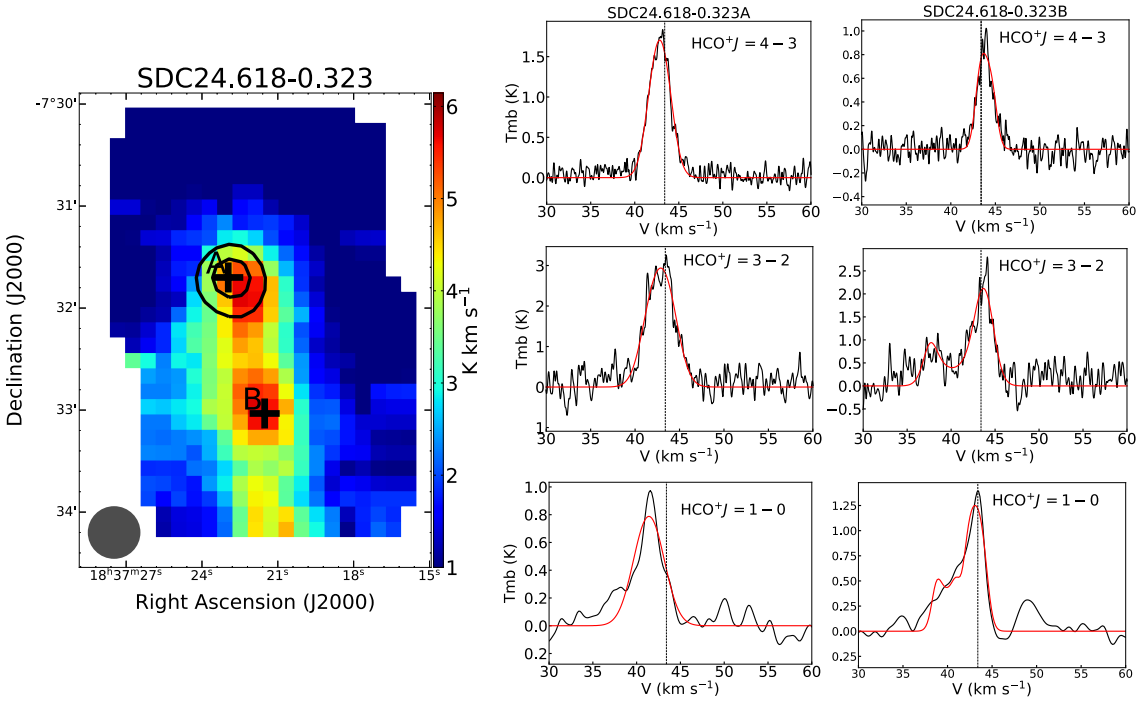

Fig. A.6 The integrated intensity map of HCO^+ J=1–0 overlaid with HCO^+ J=4–3 contours at 0.5, 0.8 and 1.0 of the maximum of the integrated intensity in K km s^{-1} for SDC24.618. The maximum of the integrated intensity has been stated in Table 5 as the biggest value of $\int T_{\rm mb} dv$ for the source. A and B are the observed positions of HCO^+ J=3–2. The *grey dot* at the corner of the emission map represents the IRAM beam size.

Vasyunina, T., Vasyunin, A. I., Herbst, E., & Linz, H. 2012, ApJ, 751, 105

Velusamy, T., Peng, R., Li, D., Goldsmith, P. F., & Langer, W. D. 2008, ApJL, 688, L87

Walker, C. K., Lada, C. J., Young, E. T., Maloney, P. R., & Wilking, B. A. 1986, ApJL, 309, L47

Wu, J., & Evans, Neal J., I. 2003, ApJL, 592, L79

Wu, J., Evans, Neal J., I., Shirley, Y. L., & Knez, C. 2010, ApJS, 188, 313

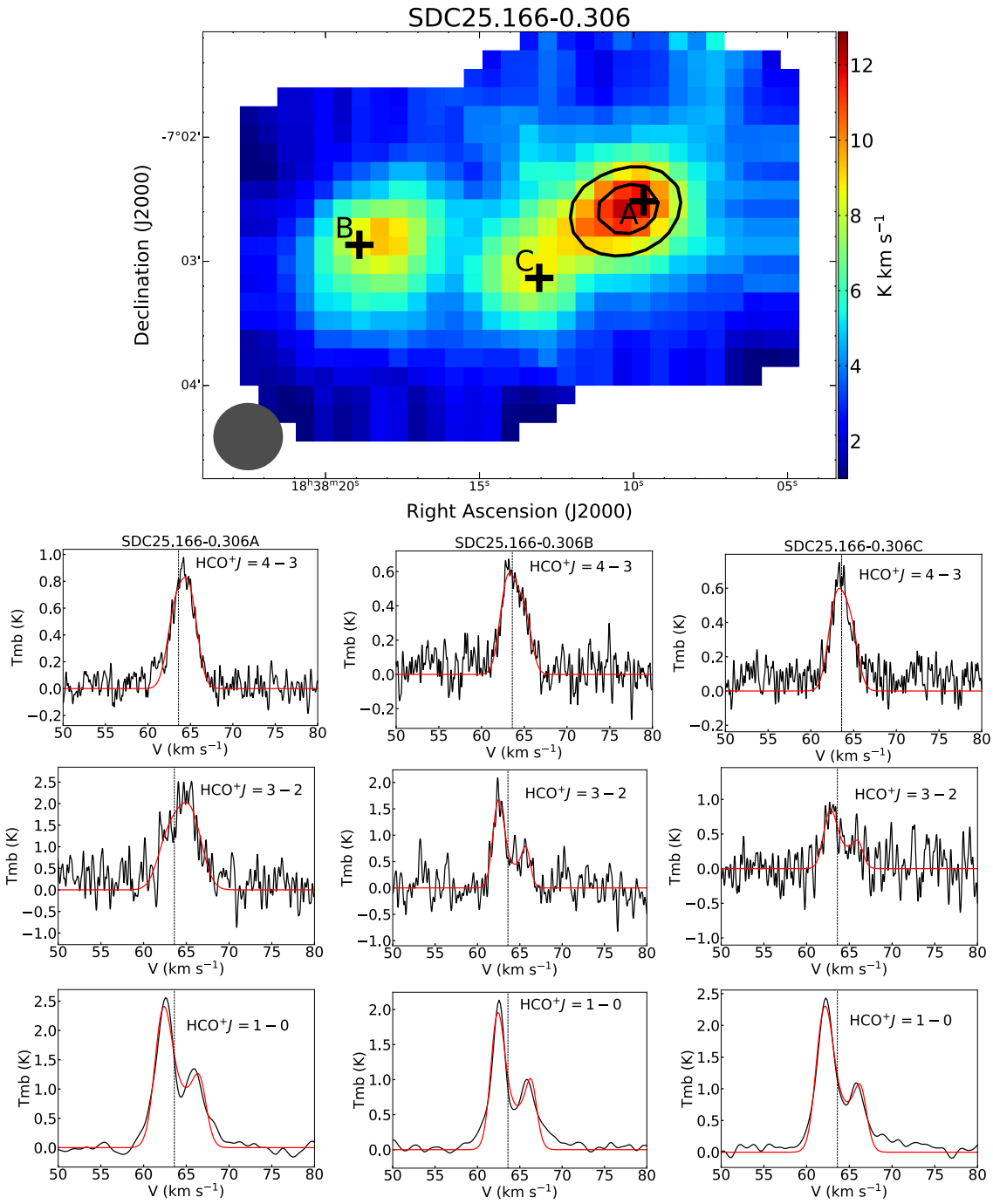

Fig. A.7 The integrated intensity map of HCO^+ J=1–0 overlaid with HCO^+ J=4–3 contours at 0.5, 0.8 and 1.0 of the maximum of the integrated intensity in K km s^{-1} for SDC25.166. The maximum of the integrated intensity has been stated in Table 5 as the biggest value of $\int T_{\rm mb} dv$ for the source. A, B and C are the observed positions of HCO^+ J=3–2. The *grey dot* at the corner of the emission map represents the IRAM beam size.

Wyrowski, F., Güsten, R., Menten, K. M., et al. 2016, A&A, 585, A149
Xie, J. J., Fuller, G. A., Li, D., et al. 2021, Science China Physics, Mechanics, and Astronomy, 64, 279511
Zhang, Q., Ho, P. T. P., & Ohashi, N. 1998, ApJ, 494, 636

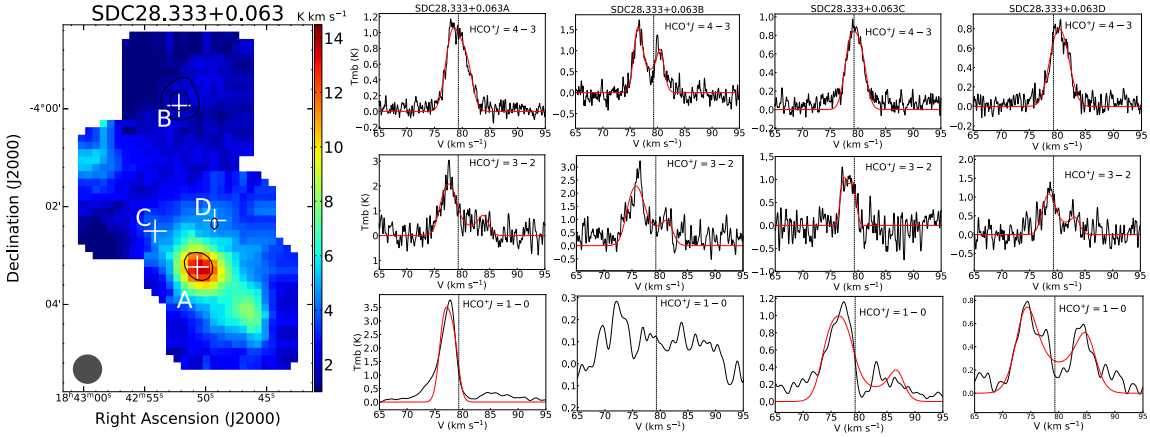

Fig. A.8 The integrated intensity map of HCO^+ J=1–0 overlaid with HCO^+ J=4–3 contours at 0.5, 0.8 and 1.0 of the maximum of the integrated intensity in K km s^{-1} for SDC28.333. The maximum of the integrated intensity has been stated in Table 5 as the biggest value of $\int T_{\rm mb} dv$ for the source. A, B, C and D are the observed positions of HCO^+ J=3–2. Note that at position B, HCO^+ J=1–0 shows no strong emission, despite position B being the emission peak for HCO^+ J=4–3 and HCO^+ J=3–2 also shows strong emission. The reasons are unknown yet. The *grey dot* at the corner of the emission map represents the IRAM beam size.

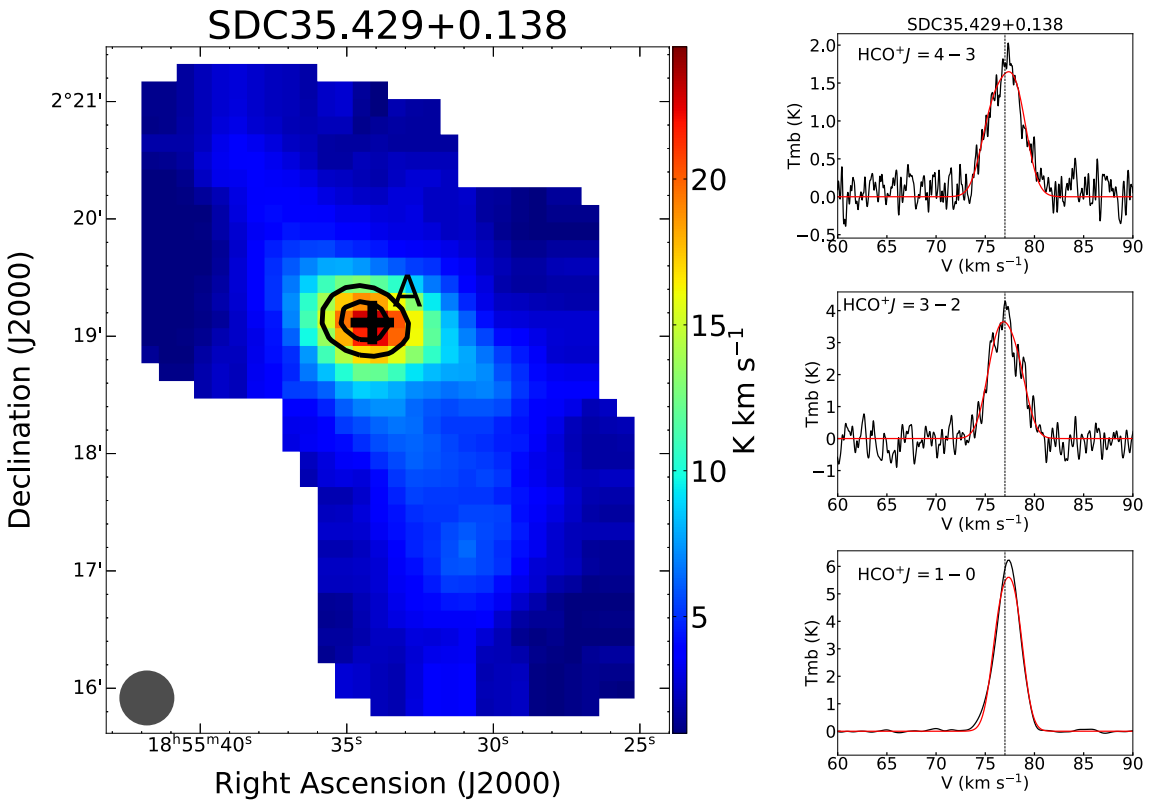

Fig. A.9 The integrated intensity map of HCO^+ J=1–0 overlaid with HCO^+ J=4–3 contours at 0.5, 0.8 and 1.0 of the maximum of the integrated intensity in K km s^{-1} for SDC35.429. The maximum of the integrated intensity has been stated in Table 5 as the biggest value of $\int T_{\rm mb} dv$ for the source. The *grey dot* at the corner of the emission map represents the IRAM beam size.

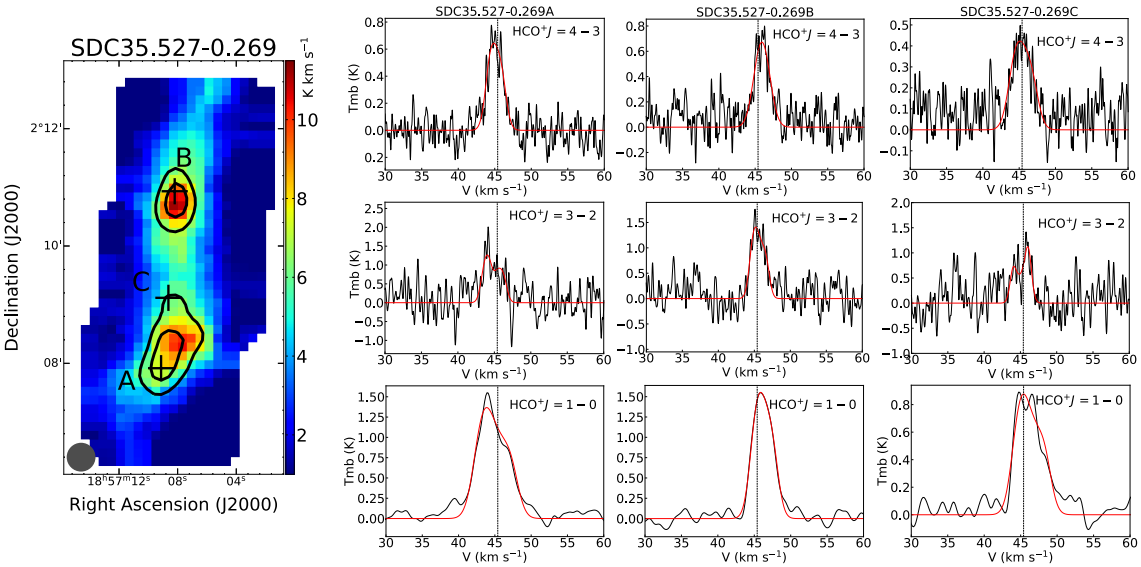

Fig. A.10 The integrated intensity map of HCO^+ J=1–0 overlaid with HCO^+ J=4–3 contours at 0.5, 0.8 and 1.0 of the maximum of the integrated intensity in K km s^{-1} for SDC35.527. The maximum of the integrated intensity has been stated in Table 5 as the biggest value of $\int T_{\rm mb} dv$ for the source. A, B and C are the observed positions of HCO^+ J=3–2. The *grey dot* at the corner of the emission map represents the IRAM beam size.

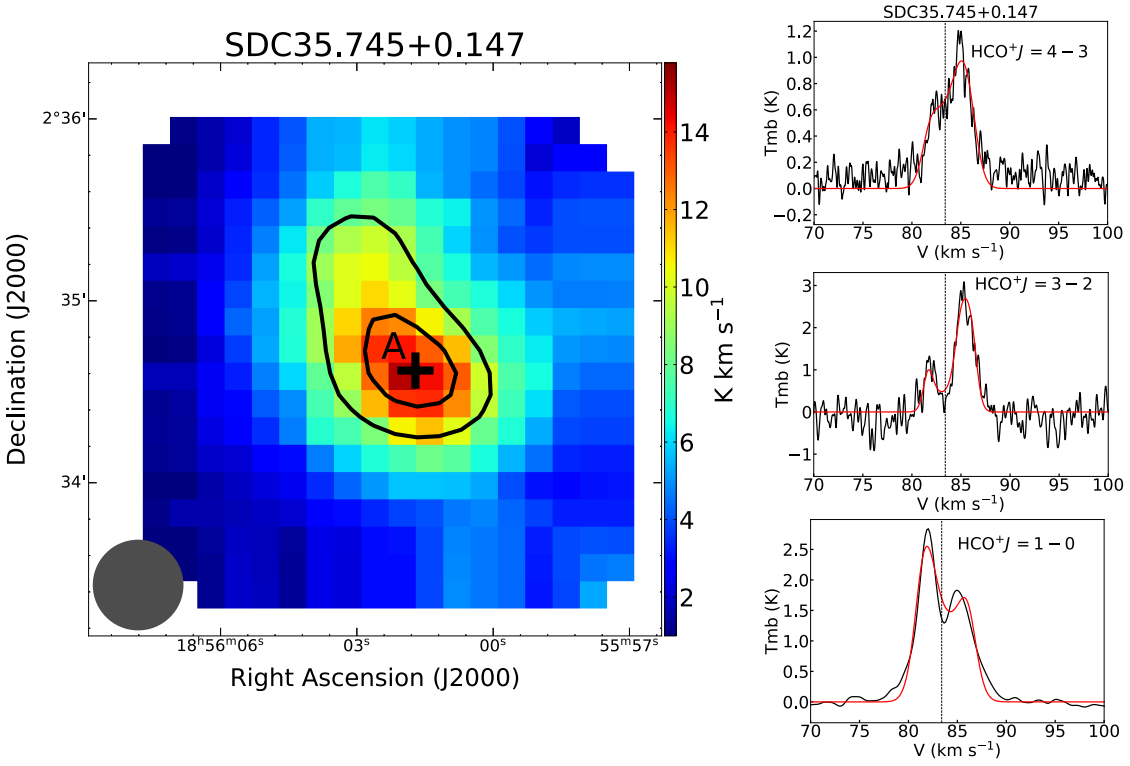

Fig. A.11 The integrated intensity map of HCO^+ J=1–0 overlaid with HCO^+ J=4–3 contours at 0.5, 0.8 and 1.0 of the maximum of the integrated intensity in K km s^{-1} for SDC35.745. The maximum of the integrated intensity has been stated in Table 5 as the biggest value of $\int T_{\rm mb} dv$ for the source. The *grey dot* at the corner of the emission map represents the IRAM beam size.